Measurement of ligand coverage on cadmium selenide nanocrystals and its influence on dielectric dependent photoluminescence intermittency

Article (Published Version)

COMMUNICATIONS CHEMISTRY

ARTICLE

https://doi.org/10.1038/s42004-019-0164-x OPEN

Measurement of ligand coverage on cadmium selenide nanocrystals and its influence on dielectric dependent photoluminescence intermittency

Aidan A.E. Fisher[1], Mark A. Osborne[1], Iain J. Day[1] & Guillermo Lucena Alcalde[1]

Photoluminescent quantum dots are used in a range of applications that exploit the unique size tuneable emission, light harvesting and quantum efficient properties of these semiconductor nanocrystals. However, optical instabilities such as photoluminescence intermittency, the stochastic switching between bright, emitting states and dark states, can hinder quantum dot performance. Correlations between this blinking of emission and the dielectric properties of the nanoenvironment between the quantum dot interface and host medium, suggest surface ligands play a role in modulating on-off switching rates. Here we elucidate the nature of the cadmium selenide nanocrystal surface, by combining magic angle spinning NMR and x-ray photoelectron spectroscopy to determine ligand surface densities, with molecular dynamics simulation to assess net ligand filling at the nanocrystal interface. Results support a high ligand coverage and are consistent with photoluminescence intermittency measurements that indicate a dominant contribution from surface ligand to the dielectric properties of the local quantum dot environment.

[1] Department of Chemistry, University of Sussex, Falmer BN1 9QJ, United Kingdom. Correspondence and requests for materials should be addressed to A.A.E.F. (email: aidan.fisher@sussex.ac.uk) or to M.A.O. (email: m.osborne@sussex.ac.uk)

Semiconducting quantum dots (QDs) have become ubiquitous across a number of applications recently including areas as diverse as solar cells[1,2], biological tags[3,4] and within the display industry[5]. Unfortunately, QDs suffer from a number of often-undesirable instabilities. One such instability is the phenomenon of photoluminescence intermittency (PI), which manifests as stochastic blinking between a bright, emissive state and a dark, quenched state at the single molecule level[6–8]. The dark state has been attributed to a number of mechanisms including multiple (non-radiative) recombination centres (MRC)[9] and diffusion-controlled electron transfer (DCET)[10]. Alternatively, the dark state can arise from QD charging and subsequent non-radiative relaxation to the valence band via an Auger quenching mechanism[11,12]. Importantly, former studies have shown that the bulk host-substrate dielectric constant, in which the QD is embedded, plays an important role in this stochastic switching process. Early work by Cichos and colleagues identified a linear correlation between the residence time of a QD in a dark state and reaction field factor, $(1-1/\varepsilon_m)$ where ε_m is the dielectric constant of the substrate or embedding medium[13,14]. Further investigations by Osborne and Fisher led to the introduction of perturbations to the host-medium dielectric constant to account for coverage of the QD surface by stabilising ligands[15,16]. In this case, an effective dielectric constant was employed to define the self-trap energies for exciton charge-carriers in the vicinity of the QD interface, in the quantitative modelling of PI using a recently advanced charge-tunnelling and self-trapping (CTST) model[15]. To better understand the interplay between PI dynamics in QDs and the dielectric properties of the QD interface, we employ high resolution magic angle spinning (HR-MAS) NMR and XPS to measure the ligand surface population and molecular dynamics (MD) simulation to gauge ligand surface coverage and its contribution to the local QD nanoenvironment.

A number of analytical methods have emerged to study a wide variety of nanoparticles including gold, palladium and platinum nanoparticles using a range of techniques such as thermogravimetric analysis (TGA), Rutherford backscattering spectroscopy (RBS) and x-ray photoelectron spectroscopy (XPS)[17]. Typically, solid specimen methods, such as RBS and XPS, are utilised to interrogate surface coverage[18,19]. Unfortunately, results from both quantitative RBS and XPS, in this instance, require careful consideration to deconvolute uncoordinated ligand from ligand attached to the QD surface.

Here, we show that ligand coverage of the QD surface derived from our analysis of HR-MAS NMR and XPS spectra is consistent with dielectric dependent PI measurements on single CdSe QDs that support a lead contribution of the ligand to the effective dielectric properties of the QD nanoenvironment within the CTST framework. The study follows in the spirit of former research pioneered by Griffin, Bawendi and Alivisatos and colleagues to approximate ligand surface coverage on CdSe QDs[20,21]. The application of HR-MAS NMR permits accurate and rapid synthesis of spectrally resolved peaks assigned to surface coordinated and uncoordinated ligand. The use of an internal standard enables simple quantitative calculations to be performed by direct peak integration. Resolution of the surface bound ligand density, ultimately, provides the basis for determining coverage of the QD by considering the conformation of the ligand at the QD surface within a self-avoiding model (Flory theory) of polymer dynamics, as well as through MD simulation. Results are used to interpret the influence of the ligand-shell on PI dynamics within the CTST framework, key aspects of which are introduced below.

Results

Charge-tunnelling and self-trapping at the QD-host interface. The photo-charging phenomenon in QDs and effects such as PI has long been a subject of interest since the early observations conducted by Brus and his colleagues[22]. Since then, a handful of models have evolved that capture the underlying photophysics. At the forefront of many of these descriptions is a tunnelling process of the exciton to trap states, either at the QD surface or externally in the supporting medium. In the latter case, this renders the parent QD charged and non-emissive due to a highly efficient Auger relaxation mechanism[23,24]. The nature of the trap state however, remains somewhat elusive. A recent study highlighted the intimate relationship between the stochastic blinking of single CdSe QDs and the substrate dielectric constant[13,14]. Notably, this may be further complicated by atmospheric effects, where it has been found that moisture in the air may passivate surface traps and alter PI blinking statistics[25], although this was not found to impact the former dielectric dependence studies on polymer substrates performed under ambient air, where even a low concentration of water molecules might be expected to dominate the local dielectric constant $(\varepsilon_{H_2O} = 80)$[13,14,16]. Osborne and Fisher further investigated the correlations between PI and the dielectric properties of the QD surround via a recently published charge-tunnelling and self-trapping (CTST) model[15,16]. In the CTST scheme (Fig. 1), the native, uncharged and emissive QD is denoted by the X_{00} state. The neutral QD may undergo stochastic transitions to either a charged core, non-emissive state ($X^+{}_{10}$) or an emissive charged surface-state ($X^+{}_{01}$) where the ejected electron is trapped by the host matrix. In the CTST nomenclature, subscripts represent the position of the exciton hole on the QD, either core (10) or surface (01), while superscripts indicate the charged state on the QD. The energetics (Fig. 1a) and kinetics (Fig. 1b) of the CTST model are formulated in terms of the QD and host-substrate macroscopic properties, namely QD size and host-dielectric properties. For example, the trapped electron is stabilised according to the host-substrate dielectric constant as alluded to by Cichos and colleagues[13,14]. Importantly, CTST simulations of PI in single QDs suggest that the surface ligands play a dominant role in dielectric effects of the medium surrounding the QD. The work herein investigates QD ligand coverage and identity using HR-MAS NMR spectroscopy and XPS to resolve both bound and unbound ligand fractions. Furthermore, the effects of altering the ligand surface coverage on PI is realised through simulation using the CTST model. At a more general level, understanding the impact of the nanoenvironment on the photophysical properties of CdSe QDs, may yield new information on the exciton dynamics for a number of systems including the recently reported perovskite QDs[26,27].

In a condensed CTST kinetic scheme (Fig. 1b), the PI is accounted for by charge-tunnelling of the photoexcited electron between the parent QD and the host matrix. Specifically, the neutral ground state QD (X_{00}) may absorb a photon, yielding the bright (X_{00}) native state. This may subsequently relax via radiative recombination producing the neutral ground state once more. Alternatively, the photoexcited neutral state (X_{00}) may undergo a stochastic transition to either a photoluminescent charged surface-state ($X^+{}_{01}$) or *dark* charged core state ($X^+{}_{10}$), which upon further excitation relaxes through a dominant Auger process. The reader is referred to the literature for a complete model description[15,16]. Importantly, for the ionised QD, the trapping potential experienced by the surface-hole state ($X^+{}_{01}$) is described using elementary electrostatic theory for a dielectric interface and the

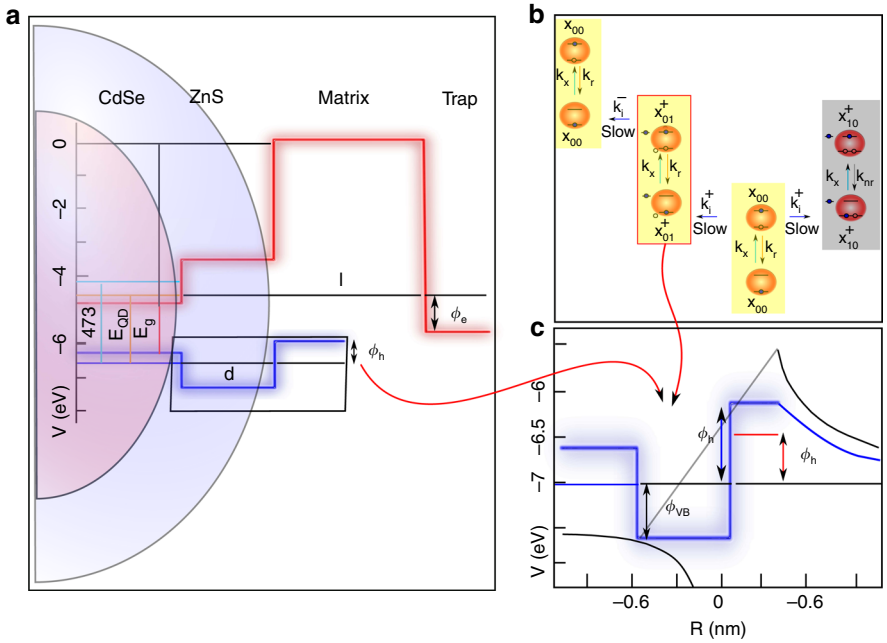

Fig. 1 Simplified energetic and kinetic scheme of the CTST model. **a** energetic scheme of the CTST framework for a general CdSe.ZnS QD. In the simplest QD system explored here, QDs were not coated with an epitaxial shell and the shell depth was set equal to zero. The band structure of the QD and trap state energies were estimated from former model iterations. In this scheme, the ground state may be excited by 473 nm light (cyan). The bulk band gap (red) and QD band gap (orange) are given by E_g and E_{QD}, respectively. The tunnelling length of the excited state electron and hole are given by l and d respectively. **b** Reduced kinetic scheme, where the neutral ground state (X_{00}) is excited with a rate constant, k_x, yielding the excited neutral state. This may relax radiatively (k_r), or undergo an ionisation process (k_i^+) to either the photoluminescent surface-charged state (X^+_{01}) or the dark core-charged state (X^+_{10}). The slow return of the electron renders the QD once again neutral and emissive. Importantly, the hole trap associated with the X^+_{01}, (red box), is influenced by the local dielectric environment. **c** The hole trap energetic profile for the charged surface-state. Note the hole trap depth ϕ_h is deeper when the surface ligands dielectric constant dominates (blue). If surface ligand effects are ignored the hole trap depth is shallower (red). Ultimately, the shallow hole trap, associated with no ligand perturbations, reduces the average potential energy barrier for electron return, k_i^-, resulting in short on times (large α_{on}) in the PI profile. This was not observed experimentally and a nanocomposite dielectric environment was found to best simulate the blinking dynamics.

method of image charges (Fig. 1a, c). At the simplest level the trapping potential is given (Gaussian units) by

$$\phi_h = \frac{Ke^2}{2r_h}\left(\frac{1}{\varepsilon_m} - \frac{1}{\varepsilon_{QD}}\right) \quad (1)$$

where the dielectric constants of the host-matrix and QD are given by ε_m and ε_{QD}, respectively, $K = (\varepsilon_{QD} - \varepsilon_m)/(\varepsilon_{QD} + \varepsilon_m)$, the fundamental charge is given by e and r_h is the hole trap radius[28]. In CTST, the surface hole trap differs from the more distant matrix-bound electron trap, since the stabilising ligands of the QD will influence the dielectric properties of the matrix in close proximity to the surface. To incorporate effects of surface ligand, ε_m is replaced with an effective dielectric constant, ε_{eff}, which is strictly a variable in CTST and generalises the self-trap energy of the hole to account for variations in the dielectric constant at the QD interface in mixed-media. HR-MAS was employed to evaluate the QD-ligand surface coverage and comparison made to CTST modelling of PI kinetics, which supports the ligand-shell as the dominant contributor to dielectric dependent QD blinking[16].

HR-MAS studies of single QD ligand density. The use of NMR has recently emerged as a spectroscopic tool for the study of QDs, where the ease of preparation compared with RBS has made NMR particularly attractive[29–31]. Furthermore, it was found that HR-MAS (Fig. 2) provided satisfactory deconvolution of the broad, pseudo solid-state signal, associated with coordinated ligand, and the sharp resonance of the free, solution phase ligand and residual non-coordinating octadecene (ODE). The spinning of the samples at a rate of 2 kHz at the magic angle removes any broadening arising from magnetic susceptibility differences due to the heterogeneous nature of the sample. A comparison between the NMR spectrum under MAS and a static solution spectrum is shown in Supplementary Fig. 1. In the case of the static solution spectrum, the bound ligand alkyl backbone signal is peak broadened and lost in the baseline. HR-MAS reduces broadening effects and an emergent bound signal is observed. No vortex effects were observed at the low spin rate. All measurements were performed at a temperature setting of 298 K, regulated by the spectrometer's variable temperature controller. The samples actual temperature at this spin rate and temperature setting is approximately 305 K as measured by an ethylene glycol thermometer[32].

To calculate the ligand density, as-synthesised core QDs were analysed using UV-Vis spectroscopy. The empirical relations outlined by Peng and colleagues[33] may be used to determine the QD concentration, number and diameter. We note that several different empirical functions can be found in the literature, each yielding subtly different QD numbers in solution. For example, Peng's relations give a QD population of 3.77×10^{15}, whereas more recent work by Jasieniak and colleagues[34] derive a QD population of 2.16×10^{15}. Work reported here employs the latter, more recent fitting parameters. The HR-MAS rotor, specifically designed to handle liquids and slurries, was subsequently loaded with a known number of QDs and an internal benzene standard. It was observed in the NMR spectra that the sharp methyl

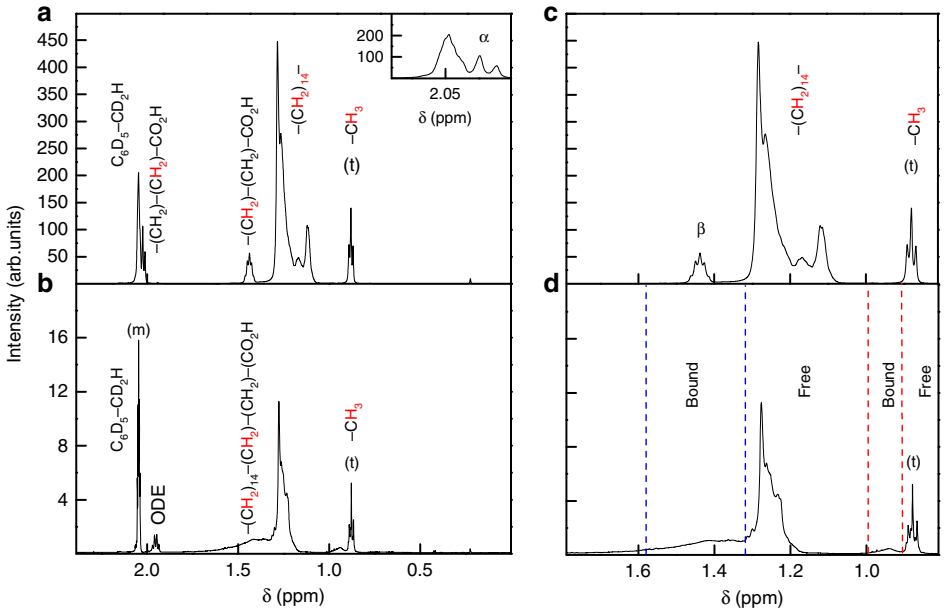

Fig. 2 1D proton NMR using MAS of free stearic acid ligand and CdSe QDs with ligand surfactant. **a** Proton NMR of the free stearic acid ligand dissolved in deuterated toluene. The triplet (0.9 ppm) was assigned as the $-CH_3$ methyl terminus of the aliphatic chain, the broad poorly resolved peak (1.2 ppm) was assigned as the $-(CH_2)_{14}-$ backbone of the long alkyl chain. The β protons appear at 1.48 ppm, while the α proton signal, inset, is at 2.03 ppm. The multiplet (2.05 ppm) arises from undeuterated toluene. **b** Proton NMR under HR-MAS of CdSe QDs in deuterated toluene. Note the broad shoulder (1.4 ppm) observed for the ligand signals, which is expected to arise from a slowly tumbling fraction of ligand bound to the QD surface. **c** Free SA ligand proton NMR, which has been expanded to show the scalar coupling. No broad downfield shoulder was detected for free SA. **d** Enlarged NMR spectrum of the CdSe QD sample. HR-MAS was employed to sharpen the broad resonance of the bound surface ligand, which appears downfield to the free ligand. This presented a unique opportunity to perform quantitative NMR using a benzene internal standard, where the broad shoulder peak area was integrated directly.

terminus resonance of the rapidly tumbling ligands displayed evidence of a broad shoulder. Typically, broad resonances may be associated with slow molecular tumbling in solution phase NMR and it was conjectured that the signal was an indication of the coordinated ligand over the NMR timescale. Moreover, it was expected that the broadening of the methyl resonance is not indicative of multiple surface binding sites since the methyl terminus is >2 nm from the QD surface in solution phase. In order to confirm the nature of the broad resonance, we performed diffusion ordered NMR (DOSY) under MAS (Fig. 3a, b) in an effort to acquire the diffusion coefficient of the detected broad fraction. The measured diffusion coefficient, for the broad resonance, may be substituted into the Stokes Einstein equation to yield an estimate of the hydrodynamic radius. In this case, a radius of 2 nm was found to be consistent with data acquired using HR-TEM (Fig. 4). The sharp resonance of the free ligand yields a hydrodynamic radius of 0.4 nm. This suggests some coiling of the free aliphatic chain in solution, where for a fully extended ligand, based on the C-C bond length (0.154 nm), we would expect a hydrodynamic radius of about $(0.154 \times 18)/2 =$ 1.4 nm for the ligand. Lastly, to reinforce these measurements, we followed in the spirit of former publications[35–37] and performed NOE under MAS, where we observed a distinctive negative NOE for the broad resonance and a positive peak for the sharp signal (Fig. 3c, d). Primarily, this arises from the dominant longitudinal relaxation pathway, where slow tumbling molecules favour the zero quantum transition pathway. In contrast, rapidly tumbling molecules, *id est* small molecules, predominantly relax via a double quantum transition. Ultimately, spectral resolution of the average free and bound ligand allows direct integration of the broad resonance and numerical calculation of the number of ligands bound to a single QD.

Attention is now turned to the composition of the ligand shell. We performed simple 1D NMR on stock octadecylamine (ODA), stearic acid (SA) and trioctylphosphine (TOP) (Supplementary Fig. 2) in a bid to detect unique NMR peaks between the various ligands. Importantly, SA exhibits a triplet (2.03 ppm), which is absent in our QD NMR spectra. This may be taken as evidence of the absence of SA in our QD samples. However, another explanation is spectral broadening of the signal, due to surface binding, and its loss in the background noise. To test this we used XPS elemental analysis. Each ligand (SA, ODA and TOP) exhibits a unique elemental binding energy (oxygen, nitrogen and phosphorus), respectively. XPS data (Supplementary Fig. 3) shows strong signals for cadmium, selenium and oxygen with no evidence of nitrogen or phosphorus. This simplifies our ligand system to exclusively SA which has a dielectric constant of $\varepsilon_{SA} = 2.2$[38].

In the case of our QD NMR samples (Fig. 2), we detect a weak isolated signal at 1.95 ppm, which may be attributed to residual non-coordinating ODE from the QD synthesis. This peak integral (0.035) is used to infer the expected peak areas for the ODE alkyl backbone and methyl protons at 1.2 and 0.9 ppm respectively. This analysis highlights that the free alkyl (1.2 ppm) and methyl (0.9 ppm) proton signals for our QD sample, are predominantly non-coordinating residual ODE (Supplementary Note 1). For simplicity, we assume no free ligand is present in subsequent calculations for the QD sample. The NMR peak integration ratio for pure SA ligand is theoretically expected to be 1:10.0 (methyl: alkyl backbone protons excluding downfield alpha protons) (Supplementary Fig. 2). Experimentally, for the bound ligand-fraction of our QD sample, we observe an integration ratio of 1:10.0 pointing toward an exclusive SA ligand surface. Hence, by exploiting the benzene internal standard we calculate a ligand surface coverage of 2.3 ligands nm^{-2} for the linear aliphatic SA chains. This appears to be in good agreement with literature estimates[31] and supports findings from our XPS measurements.

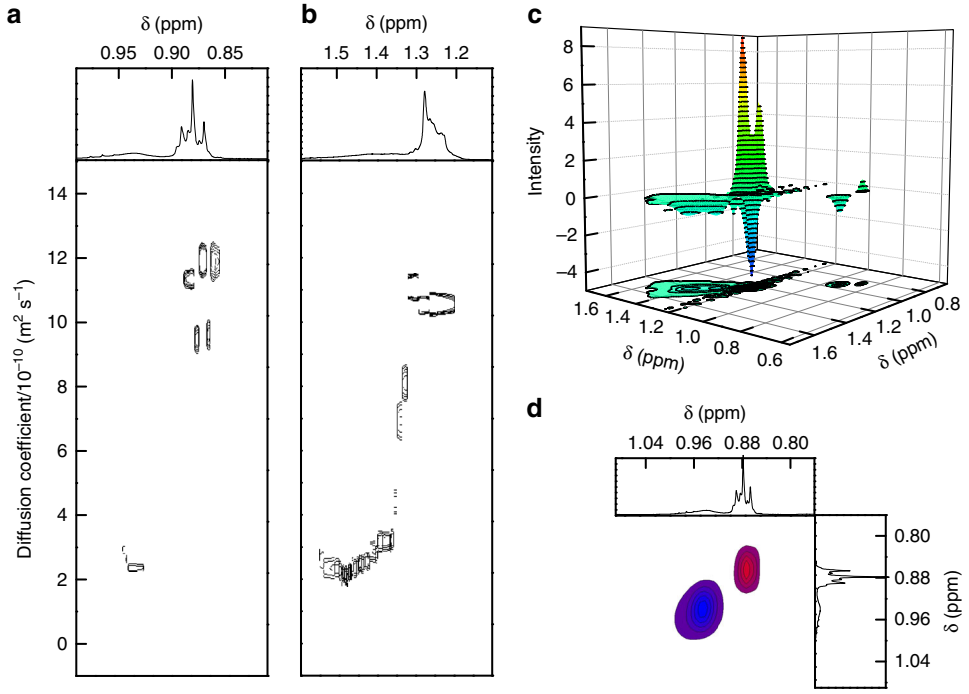

Fig. 3 Deconvolution of the free and bound ligand on CdSe QDs using diffusion NMR and NOE techniques. **a** DOSY spectrum under MAS of the ligand methyl resonance. The sharp resonance of the triplet, associated with free ligand/residual ODE, diffuses at about 12×10^{-10} m^2 s^{-1}. Importantly, the broad shoulder at 0.95 ppm is associated with bound ligand diffusing at approximately 2×10^{-10} m^2 s^{-1}. The Stokes Einstein equation was employed to estimate QD size from the diffusion data yielding a hydrodynamic radius of 2 nm. **b** the alkyl backbone of the ligand similarly exhibits sharp and peak broadened resonances, which may be ascribed the free/residual ODE and bound ligand, respectively. **c** NOE spectrum of the CdSe QDs under MAS. The methyl resonance decomposed into both a positive (red) and negative (blue) NOE phase evidencing a rapid and slowly tumbling ligand population, respectively. **d** detailed NOE contour spectrum under MAS emphasising the methyl resonance. The sharp resonance (positive NOE) and broad shoulder (negative NOE) highlight the rapid tumbling of the free ligand/residual ODE (red) and slow tumbling of the bound ligand (blue).

To further evaluate the ligand density, the density of a single CdSe QD crystal was calculated using diffraction data (Supplementary Fig. 4) and HR-TEM images (Fig. 4 and Supplementary Fig. 5). The number of CdSe ion pairs was then determined using the following relationship

$$\frac{V_{\mathrm{QD}}\rho_{\mathrm{CdSe}}}{M_{r\mathrm{CdSe}}}N_{\mathrm{A}} = 249\ \text{ion pairs} \qquad (2)$$

where V_{QD} is the volume of a single QD, the density of the QD is given by ρ_{CdSe}, the molecular weight is $M_{r\mathrm{CdSe}}$ and N_{A} is the Avogadro constant. The number of surface atoms coordinated to ligand was then approximated using a spherical cluster analysis. It can be shown, that for a cluster size of about 500 atoms (249 CdSe ion pairs), 45% of the atoms reside at the crystal surface (Supplementary Note 2). Assuming a crystal stoichiometry of approximately (1:1 = Cd:Se), as verified by inductively coupled plasma mass spectroscopy (ICP-MS) (Supplementary Fig. 6), then approximately 225 atoms (Cd + Se) exist at the QD surface, where a single QD accommodates about 65 SA ligands. Thus, one may naively assume one quarter coverage of the QD surface on a ligand per atom basis, leaving the surface largely exposed to intrusion by the host-embedding medium. However, results from CTST simulations agree somewhat poorly with experimental data when the dielectric constant of the QD surrounding-medium approaches that of the host-matrix alone[16]. To interpret this discrepancy we develop arguments using former communications, which report the effects of ligand folding dynamics of aliphatic amines. Strouse and colleagues[29] made use of ^{77}Se ^{1}H heteronuclear correlation (HETCOR) NMR to investigate the interaction between the alkyl backbone of hexadecylamine (HDA) and surface selenium sites. The authors showed evidence of significant chain tilting towards the QD surface, where a total of five selenium surface sites were found to interact with the alkyl chain. Generally, photoluminescence studies on single QDs are performed in the solid state and it is reasoned here that the absence of solvent will accentuate collapse of the ligand onto the QD surface. Moreover, studies on surface coverage in the solid state, conducted by Rosenthal and colleagues[19] using RBS, revealed the surface coverage to be in excess of 70%, where the surface ligand was a sterically bulky trioctylphosphine oxide (TOPO) ligand. Importantly, in the PI studies performed here, we found our CTST simulations were in agreement with experiment when a value of the effective dielectric constant, $\varepsilon_{\mathrm{eff}}$, close to that of the ligand, was employed. Hence, we argue from our own data, and the findings of Strouse and Rosenthal, that ligand coverage should fill at least 70% of the surface, where in this case the QD is efficiently wrapped by the long aliphatic chain of SA.

Indeed it was found that within a modified-CTST model used to describe the shell-thickness dependent blinking statistics in core-shell CdS capped CdSe QDs, a ligand filling of almost 100% was required to faithfully reproduce trends in the power-law exponents and cut-off times with increasing CdS monolayers[15]. Again, the result highlights the need to consider ligand conformation on the QD surface when correlating coverage, as measured in solution phase, with photoluminescent (PL) blinking statistics measured under dry, ambient conditions.

QD blinking and effects of the nanoenvironment. Complete filling of the QD surface by collapse of the ligand is not wholly unexpected, given the long C_{18} backbone of the dominant SA [$CH_3(CH_2)_{16}CO_2H$], even at only 28% surface atom coverage (65 SA per 225 atoms). Within a self-avoiding model of polymer

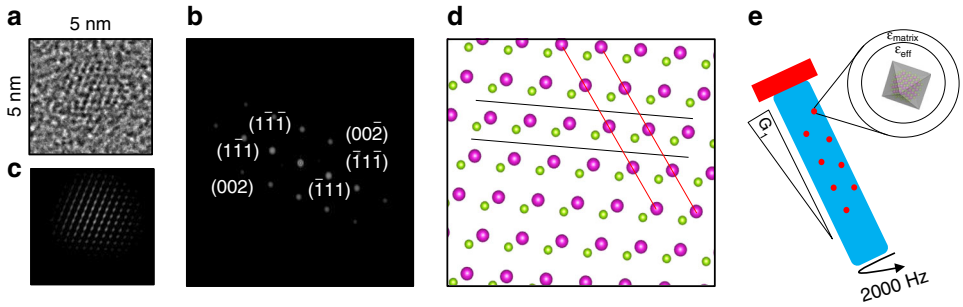

Fig. 4 HR-TEM image and lattice reconstruction of as-prepared CdSe QDs for use in NMR surface ligand density studies. **a** high resolution image of a single CdSe QD of diameter 3 nm. This QD size was used to estimate the number of surface atoms from Eq. (2) and hence ligand density. **b** reciprocal space image of the CdSe QD viewed along the [110] zone axis. **c** reconstructed real space lattice after noise filtering of the reciprocal lattice. **d** CdSe zinc blende atomic model (ICSD:620439) of the (110) lattice facet. The density of the zinc blende phase (5.66 g cm^{-3}) was calculated and used in Eq. (2) to estimate the number of surface atoms. The red and black lines highlight the (002) and ($\bar{1}$11) planes, respectively. The purple and green spheres represent selenium and cadmium lattice positions respectively. **e** schematic of the QDs dispersed in deuterated toluene undergoing NMR under MAS. The effective dielectric constant and matrix dielectric constant around the QD (ICSD:620439) are given as ε_{eff} and ε_{matrix}, respectively. At the QD surface, coordinated ligands, resolved by NMR, modify the matrix dielectric constant, which leads to subtle perturbations in the hole trap depth defined by Eq. (1).

dynamics we can use the Flory radius, $R_F = l(d/3)^{\nu/3}N^{\nu}$, to estimate the area covered by a ligand, where $l = 0.154$ nm is the C-C bond-length, $N = 18$ is the number of carbon units and $\nu = 3/(d+2)$ is the Flory exponent for a conformational space of dimension d[39]. For tethered polymers the Flory exponent has been found to vary from the 3D to 2D limits, $\nu = 3/5$ and $\nu = 3/4$, respectively, with increasing surface interaction[40]. Using the 3D limit as a lower bound a single ligand has a footprint of $\pi R_F^2 \simeq 2.4\,\mathrm{nm}^2$, giving a total surface coverage of 156 nm^2 for 65 SA per QD. For a mean QD radius of 1.5 nm and surface area $4\pi R_{QD}^2 \simeq 28\,\mathrm{nm}^2$, the ligand represents an >5× coverage of the surface. The excess is similarly significant from an atomistic perspective, with the 65×C_{18} atoms again representing more than five-fold the number of surface atoms. As such relaxation of the ligand at the QD surface would be expect to provide more than monolayer capping of the surface. We illustrate this possibility with results from MD simulations (ChemSite Pro, ChemSW) of SA ligands on a CdSe surface (Fig. 5a, b). The simulation was reduced to a 4 × 4 array (5.76 nm^2) of the CdSe zinc-blend unit cell with 13 associated SA molecules (2.3 ligands nm^{-2}) to represent closely the NMR measured ligand densities. From an extended, "standing" start (Fig. 5a), the ligand conformation expected from swelling in the organic NMR solvent, SA molecules were relaxed at constant temperature (300 K) under periodic boundary conditions and without dielectric solvation to represent the ambient air under which PL blinking studies have been performed. We found the SA ligand backbone readily condensed with signficant coverage of the QD surface, with typical exposures of only 2–3 CdSe units of the 32 surface pairs corresponding to >90% filling at the QD interface (Fig. 5b).

The nature of the QD surface effects the range of PL-on and off switching rates in the QD PL intensity trajectory (Fig. 5c), as characterised by the probability density distribtuions (PDDs) of on and off-times extracted (Fig. 5d) by threshold analysis[16]. In the CTST model the effective dielectric constant influences QD PL-blinking through a dependency of the electron and hole tunnelling potentials on the self-trap energies of the charge-carriers in the host and at the QD surface, respectively. Specifically, the dependence of electron and hole trapping energies on the permitivity of the QD nanoenvironment, in this case ε_{eff}, gives rise to barrier heights that increase as $V_{on/off} = A - B/\varepsilon_{eff}$ with increasing dielectric constant (Fig. 5e), where constants A and B are functions of the electron affinity and the QD band gap (Supplementary Note 3). For electron recombination in the surface-charged, on-state, $X^+{}_{01}$, additional stabilisation of the hole at the QD-surface, raises the overall barrier and reduces the downhill tunnelling gradient compared to electron return to the valence band hole in the core-charged, off-state, $X^+{}_{10}$. The effect on PI statistics is to increase the range of PL-on and off times with increasing ε_{eff}, as characterised by the decreasing exponents α_{on} and α_{off} of the truncated power-law (TPL), $P(t) = At^{-\alpha_{on/off}}e^{-\Gamma t}$, commonly used to describe the on and off-time PDDs (Fig. 5f). The saturation rate in the exponential component defines a cut-off time, Γ^{-1} at which the PL blinking statistics no longer follow power-law behaviour and is generally most evident in on-time distributions. Within the CTST framework, cut-off in the on-times evolves from a biexciton mechanism that leads to quenching of the $X^+{}_{01}$ on-state by recombination of a hot-electron at the surface trapped hole. Here, the net rate of biexciton formation (within the exciton lifetime) is given by k_x^2/k_r, where the excitation and radiative relaxation rate constants k_x and k_r depend on the local field produced by the QD-ligand dielectric mismatch ($\varepsilon_{QD} \sim 9\varepsilon_0$ vs $\varepsilon_{eff} \sim 2\varepsilon_0$). Ultimately this leads to a cut-off rate that scales as the square of the local field factor, $F = 3\varepsilon_{eff}/(\varepsilon_{QD} + 2\varepsilon_{eff})$ and a cut-off time that increases near-linearly with $1/\varepsilon_{eff}$ (Fig. 5e inset). We find an effective dielectric constant $\varepsilon_{eff} = 2.2$, corresponding to that of the SA ligand, provides a best fit of simulated on- and off-time PDDs and associated TPL parameters to those derived from experiment. The dielectric constant is consistent with the model of ligand condensation and collapse at the QD surface. Values $\alpha_{on} = 1.64 \pm 0.18$ and $\alpha_{off} = 1.59 \pm 0.14$ compare favourably (within error) with those obtained by Isaac et al.[13] for TOPO stabilised core CdSe QDs in low dielectric polymeric media (1.56 and 1.62 respectively in p-terphenyl, $\varepsilon_m = 2.1$), although the authors observe a weaker inverse dielectic dependence of α_{off} on the dielectric environment than the CTST model immediately suggests and α_{on} was observed to be almost independent of host permitivity. However, for the range of QD host matrices analysed, with dielectic constants spanning $\varepsilon_m = 2.1$ (p-terphenyl) to 14 (PVA), we note that given TOPO and SA ligands have closely related dielectric constants (2.5 and 2.2, respectively), the effective constants reduce to the range, $\varepsilon_{eff} = 2.2$ to 3.4, assuming a simple mean of ligand and host-dielectric constants and the lower estimate of 90% surface coverage obtained from our simulations. In this case, the corresponding values of $\alpha_{off} = 1.62$ and 1.38 (from ref. [13]) for these reduced ε_{eff} constants now fall in line with those predicted by the CTST model (Fig. 5f, blue dotted line), although corresponding on-time exponents $\alpha_{on} = 1.56$ and 1.58 remain less sensitive to ε_{eff} than expected from CTST. We further

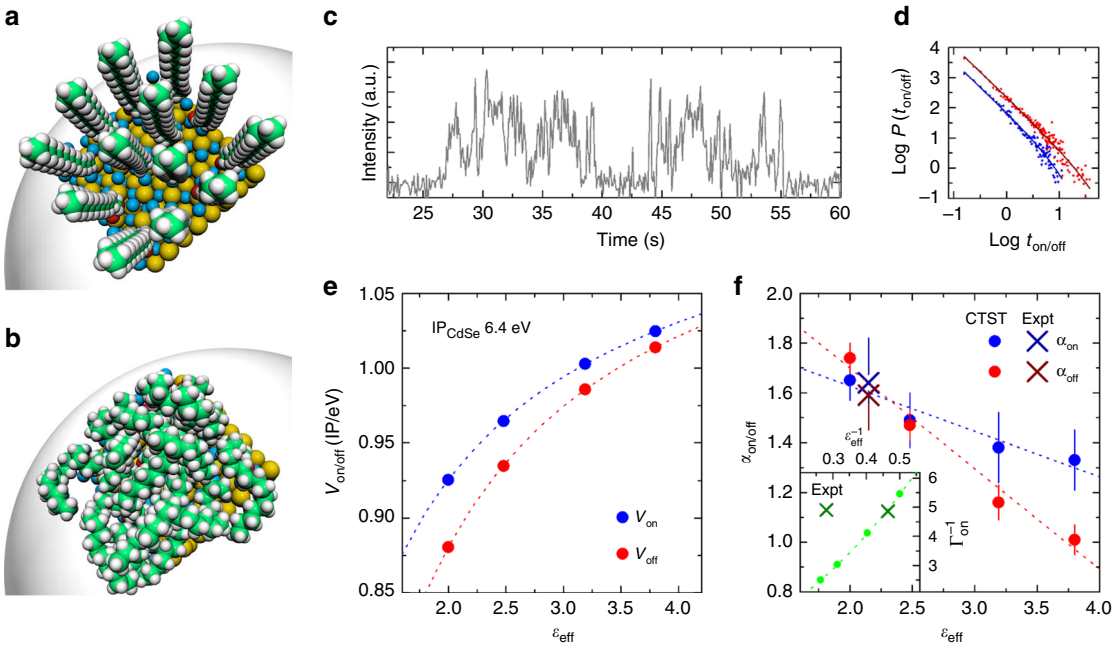

Fig. 5 QD-ligand surface coverage from MD simulation and CTST analysis of PI in CdSe. **a** Representation of SA molecules in extended conformations on a 4 × 4 supercell CdSe surface, at a density of 2.3 ligands nm^{-2} and **b** following relaxation of ligands under ambient, non-solvated conditions at constant temperature (300 K) with periodic boundary conditions. In the extended ligand conformation a significant fraction of the CdSe surface is exposed (with 13 ligands per 32 CdSe surface pairs), while in the collapsed state much of the surface is filled by the ligand backbone. **c** Extract of a single QD PL intensity trajectory from a sample of the same core-QDs analysed by NMR and **d** the corresponding on-times (blue) and off-times (red) PDDs compiled from 20+ individual QDs. **e** Dependence of the CTST mean electron tunnelling barrier potentials V_{on} and V_{off} on the effective dielectric constant of the QD nanoenvironment. The $A-B/\varepsilon_{eff}$ scaling (dotted lines with blue on, red off) in each case ($A_{on/off} \simeq 7.37/7.44$, $B_{on/off} \simeq 3.0/3.6$), arises from the self-energies that define the charge-carrier traps, notably the hole stabilisation energy ϕ_h (see text). **f** Dependence of TPL (see text) parameters α_{on} and α_{off} on ε_{eff}. Error bars generated from fits to 30 on/off PDDs derived from CTST simulations. Inset: dependence of truncation time,Γ_{on}^{-1} as defined in the CTST model on ε_{eff}^{-1} (inset). Dotted lines represent linear least squares fit to α_{on} (blue), α_{off} (red) and Γ_{on}^{-1} (inset green).

note that while our experimentally derived truncation time, $\Gamma_{on}^{-1} = 4.8 \pm 3.0$ is subject to large error and differs from typical values (1.2–1.8) measured by Isaac et al., it is does fit within the ε_{eff} dependent local field factor that governs the biexciton generation and surface-hole quenching associated with the suppression of long on-times in the CTST model. In sum the results suggest an effective dieletric constant, ε_{eff}, which accounts for a signficant coverage of the QD surface by ligand and restricted exposure to the QD host substrate or embedding medium, is a relevant quantity in the analysis of QD optical properties in different dielectric environments.

To conclude, this communication has investigated the nature of single QD surfaces using HR- MAS to provide a quantitative measure of the average number of ligand molecules bound to the QD surface. Measured ligand densities have been used to estimate the QD ligand coverage, following condensation at the QD surface, through MD simulation. Finally, ligand coverage was used to interpret PI in single QDs within the CTST framework. Comparison between simulation and experiment found the CTST model consistent with QD blinking kinetics that are dependent on dielectric properties at the QD-surface, where the dominant contributor to the effective dielectric constant is the stabilising ligand.

Methods

Chemicals. Cadmium oxide (CdO) 99.5% trace metals basis, stearic acid (SA) 95% reagent grade, 1-octadecene (ODE) 90% technical grade, octadecylamine (ODA) 90% technical grade, trioctylphosphine (TOP) 90% technical grade and toluene-d_8 99 atom % D were sourced from Sigma-Aldrich. Selenium 99.999% 200 mesh was sourced from Alfar Aesar. Ethanol and methanol was sourced from VWR. Chemicals were used without further purification.

Synthesis of CdSe QDs. Zinc-blende QDs were produced using a modified literature protocol[41]. Briefly, a three neck round bottom flask was infused with cadmium oxide (35 mg), stearic acid (0.35 g), 1-octadecene (4 mL) and a magnetic stir bar. A vacuum was applied to the sealed vessel for 15 mins followed by an argon stream. The mixture was heated to 240 °C and the temperature maintained until a clear colourless solution formed. The mixture was then cooled to room temperature and octadecylamine (1.4 g) was added. The flask was degassed and backfilled with argon. The mixture was subsequently heated to 270 °C for the injection the selenium precursor.

The selenium precursor was prepared by dissolving selenium powder (0.12 g) in trioctylphosphine (2 mL). The rapid injection of the selenium precursor into the hot cadmium mixture induced QD nucleation, indicated by an immediate colour change from clear and colourless to yellow/red. Growth of the QDs proceeded for two minutes at 250 °C before cooling to room temperature. Flocculation of the QDs was achieved by the addition of a methanol/ethanol anti-solvent. The resulting suspension was centrifuged at 3000 rpm for 30 mins. The supernatant was discarded and the QD solid dissolved in deuterated toluene.

Single molecule photoluminescent studies. Photoluminescence experiments were conducted using an inverted optical microscope (Nikon, Eclipse TE2000, Japan) equipped with a high numerical aperture objective lens (Nikon, Plan Apo, 60x, NA 1.45, Japan). Excitation light from a CW laser (473 nm Scitec Instruments, UK) was passed through a quarter-wave retarder before being focussed into the back aperture of the objective lens via a 200 mm plano-convex lens. Through objective total internal reflection (TIR) was achieved by tilting the excitation beam off-axis. The excitation light and sample photoluminescence was separated by employing a dichroic mirror (Semrock, FF509-Di01, USA). The light collected from the QDs was subsequently passed through an emission filter (Semrock, Brightline 609/54, USA) before being projected onto a chilled ICCD camera (Princeton Instruments, PI-Max Gen 3). The data was collected using a camera integration time of 80 ms and a beam excitation power of ~100 W cm^{-2}, after accounting for near-field enhancement. Laser powers were kept low to minimise any photo-oxidation effects. Typically, QD blinking profiles were acquired for at least 12,000 frames after which the QDs underwent significant photobleaching. Image focus was maintained with the assistance of a bespoke feedback loop, which monitors the *z*-plane stage displacement. The focus was restored using a motorised focus drive and control hub (Prior Scientific, Proscan 2, UK). The colloidal QD

dispersions were spun cast 3000 RPM onto a flame-cleaned coverslip (Menzel Glaser, 22 × 40, 1.5, EU), where QD concentrations were adjusted to produce a desirable density of about 0.1 QD μm^{-2} for single molecule measurements.

Image processing and data analysis. Collected image stacks of single QDs were analysed using ImageJ and a customised photoluminescence intermittency algorithm. Essentially, the algorithm detects and crops about single photoluminescent QDs. The QD grey-scale counts were then plotted in the temporal domain to produce the intensity trajectory. The photoluminescently quenched dark state was distinguished from the bright state by establishing a threshold, where we adopt a threshold of 2σ above the background as is common within the literature. Furthermore, it was noted that grey-states were rare within the trajectory profiles and a separate treatment of these borderline intensity states was not required. This is shown in (Supplementary Fig. 7). In this case, the grey state of bare CdSe QDs is only weakly modulated and is approximately the same intensity as the on state. In contrast, core-shell CdSe.CdS QDs exhibit a deeply modulated grey state, which approaches the on-off threshold for blinking analysis. The grey states arise naturally from the CTST description, where the excess hole equilibrium is shifted toward the core for thick shell QDs. This manifests as low intensity grey states over the camera exposure time. Since we investigate only bare CdSe QDs in detail, which show well-defined on/off states, we use the simple 2σ threshold to separate on and off events. The probability density distribution was calculated using the method outlined by Nessbitt and colleagues[7] given by $P(t) = 2N_i/[(t_{i+1} - t_i) + (t_i -; t_{i-1})]$, where N_i is the number of occurrences of the bright or dark event of duration t_i while t_{i+1} and t_{i-1} represent the durations of the proceeding and preceding events, respectively. The PDD data were aggregated for a minimum of 30 individual QDs and the data was fitted using a truncated power law (TPL), $P(t) = At^{-\alpha}e^{-t/\tau_c}$, where fitting parameters α and τ_c were varied using a Leven-Marquardt algorithm for nonlinear least-squares minimisation.

UV-Vis measurements. UV-Vis data was obtained using a Thermo Scientific UV300 spectrometer. The data was collected using a 1 nm data interval across a single scan cycle at 240 nm/min.

NMR methods. NMR measurements were performed using a Varian VNMRS 600 spectrometer. All magic angle spinning experiments employed a 4 mm HR-MAS gHX Nano probe equipped with a magic angle gradient coil, producing up to 138 G cm^{-1}. The spectrometer temperature was regulated at 298 K for all measurements with an actual sample temperature at low spin speeds of 305 K as calibrated using an ethylene glycol thermometer. The 1D NMR and NOESY data was processed using the MestreNova software. The raw DOSY data was processed using the DOSY toolbox[42].

1D proton HR-MAS NMR was produced at a ^{1}H frequency of 599.7 MHz with a spectral width of 9615 Hz, 32768 data points with up to 128 transients. Quantitative measurements were performed at a spin rate of 2 kHz using a small flip angle pulse enabling more rapid recycling of the magnetisation (recycle delay 1 s). An inversion recovery experiment was performed to determine the T1 of the slowest relaxing signal (0.74 s). The inter-pulse separation (recycle delay + acquisition time) was at least five times longer than the slowest relaxing signal.

2D HR-MAS DOSY NMR was generated using the One-shot pulse sequence[43], which reduces problematic eddy currents and does not require phase cycling. Importantly, the diffusion delay was 50 ms, the diffusion encoding gradient pulse was 1 ms, and a total of 15 gradient amplitudes were used from 5.09 G cm^{-1} up to 80.1 G cm^{-1}. An imbalance factor of 0.2 was using for all experiments. The pulse sequence delays were rotor synchronised, with the spin rate being 2 kHz. The data was subsequently analysed using the modified Stejskal-Tanner equation in order to synthesise the 2D spectra.

HR-MAS NOESY NMR was achieved using a zero-quantum filter pulse sequence. The mixing delay was 200 ms with a relaxation time of 1 s using 200 t_1 increments. Measurements were recorded at a spin rate of 2 kHz.

TEM techniques. High resolution TEM, high angle annular dark field and energy dispersive x-ray analysis was performed using an FEI Technai Osiris S/TEM equipped with an FEI extreme Schottky field-assisted thermionic emitter. EDX maps were acquired from four Bruker silicon drift detectors arranged about the central beam axis leading to a collection solid angle of about 0.9 sr. The electron beam was scanned over the sample with a dwell time of 200 ms/pixel.

HR-TEM images were captured using a Gatan Ultrascan 1000XP (2048 × 2048 pixels) camera with a high-speed upgrade. The images of the QDs were acquired at near-Scherzer defocus in order to maximise spatial resolution. The HR-TEM images were processed using the ImageJ software to generate fast Fourier transforms of the raw images.

X-ray diffraction. X-ray diffraction was performed using a Siemens D500 powder x-ray diffractometer using copper K-alpha radiation (0.154 nm) operating at 40 kV and 30 mA. The CdSe QDs were ground into a powder using a pedestal and mortar to form a fine powder.

Inductively coupled plasma mass spectroscopy. Typically, CdSe QDs were dissolved using concentrated nitric acid overnight. The concentrated solution was diluted a 10-fold prior to ICP-MS. Stoichiometric measurements were carried out using an Agilent 7500ce series ICP-MS operating in helium collision mode. All ICP-MS calibration standards were purchased from Sigma-Aldrich.

X-ray photoelectron spectroscopy. Samples were analysed using a Thermo Scientific K-alpha XPS instrument equipped with a micro-focused, monochromatic Al x-ray source. The Al x-ray source was operated at 12 KeV using a 400-micron spot size. A constant analyser energy of 200 eV was used for survey scans and 50 eV for detailed scans. A low energy/ion flood source was used to achieve charge neutralisation.

QD blinking simulation algorithm. Stochastic simulations within the CTST framework were accomplished using a standard Gillespie algorithm. Importantly, the algorithm is well suited to describe the highly distributed QD kinetics and stochastically models both the residence time in a given state and transitions out of the current state. The simulated kinetics were advanced in time by sampling from an exponential distribution according $\tau = -\ln(u_1)/r_0$ where τ is the incremental time step, u_1 is a random number in the interval (0/1) and r_0 is the sum of all transitions out of the current state. The state, to which the QD transitions, is evaluated according to the condition $\sum_{i=1}^{m} r_i < r_0 u_2 \leq \sum_{i=1}^{m+1} r_i$ where u_2 is a random number in the interval (0/1) and r_i is the i^{th} transition out of the current state. The simulation parameters were updated following each iteration and the procedure repeated. On and off-times were extracted from simulated PL intensity trajectories and PDDs constructed using the same procedures applied in the analysis of experimental PL trajectories. The key parameters α_{on}, α_{off} and τ_c, describing the QD-blinking statistics were obtained by non-linear least squares fit of the TPL to the PDDs as per experimental profiles.

Data availability

Materials, data and codes are available upon request from the corresponding authors.

Received: 16 November 2018 Accepted: 17 May 2019
Published online: 07 June 2019

References

1. Huynh, W. U., Dittmer, J. J. & Alivisatos, A. P. Hybrid nanorod-polymer solar cells. *Science* **295**, 2425–2427 (2002).
2. Shen, Q., Kobayashi, J., Diguna, L. J. & Toyoda, T. Effect of ZnS coating on the photovoltaic properties of CdSe quantum dot-sensitized solar cells. *J. Appl. Phys.* **103**, 084304 (2008).
3. Gao, X., Cui, Y., Levenson, R. M., Chung, L. W. & Nie, S. In vivo cancer targeting and imaging with semiconductor quantum dots. *Nat. Biotechnol.* **22**, 969–976 (2004).
4. Wu, X. et al. Immunofluorescent labeling of cancer marker Her2 and other cellular targets with semiconductor quantum dots. *Nat. Biotechnol.* **21**, 41–46 (2003).
5. Jang, E. et al. White-light-emitting diodes with quantum dot color converters for display backlights. *Adv. Mater.* **22**, 3076–3080 (2010).
6. Frantsuzov, P., Kuno, M., Janko, B. & Marcus, R. A. Universal emission intermittency in quantum dots, nanorods and nanowires. *Nat. Phys.* **4**, 519–522 (2008).
7. Kuno, M., Fromm, D., Hamann, H., Gallagher, A. & Nesbitt, D. J. "On"/"off" fluorescence intermittency of single semiconductor quantum dots. *J. Chem. Phys.* **115**, 1028–1040 (2001).
8. Neuhauser, R., Shimizu, K., Woo, W., Empedocles, S. & Bawendi, M. Correlation between fluorescence intermittency and spectral diffusion in single semiconductor quantum dots. *Phys. Rev. Lett.* **85**, 3301–3304 (2000).
9. Frantsuzov, P. A., Volkán-Kacso, S. N. & Jankó, B. R. Universality of the fluorescence intermittency in nanoscale systems: experiment and theory. *Nano Lett.* **13**, 402–408 (2013).
10. Tang, J. & Marcus, R. Mechanisms of fluorescence blinking in semiconductor nanocrystal quantum dots. *J. Chem. Phys.* **123**, 054704 (2005).
11. Bae, W. K. et al. Controlled alloying of the core–shell interface in CdSe/CdS quantum dots for suppression of Auger recombination. *ACS Nano* **7**, 3411–3419 (2013).
12. Efros, A. L. & Rosen, M. Random telegraph signal in the photoluminescence intensity of a single quantum dot. *Phys. Rev. Lett.* **78**, 1110–1113 (1997).
13. Issac, A., Krasselt, C., Cichos, F. & Von Borczyskowski, C. Influence of the dielectric environment on the photoluminescence intermittency of CdSe quantum dots. *ChemPhysChem* **13**, 3223–3230 (2012).

14. Issac, A., Von Borczyskowski, C. & Cichos, F. Correlation between photoluminescence intermittency of CdSe quantum dots and self-trapped states in dielectric media. *Phys. Rev. B* **71**, 161302 (2005).
15. Fisher, A. A. E. & Osborne, M. A. Sizing up excitons in core–shell quantum dots via shell-dependent photoluminescence blinking. *ACS Nano* **11**, 7829–7840 (2017).
16. Osborne, M. A. & Fisher, A. Charge-tunnelling and self-trapping: common origins for blinking, grey-state emission and photoluminescence enhancement in semiconductor quantum dots. *Nanoscale* **8**, 9272–9283 (2016).
17. Smith, A. M., Johnston, K. A., Crawford, S. E., Marbella, L. E. & Millstone, J. E. Ligand density quantification on colloidal inorganic nanoparticles. *Analyst* **142**, 11–29 (2017).
18. Katari, J. B., Colvin, V. L. & Alivisatos, A. P. X-ray photoelectron spectroscopy of CdSe nanocrystals with applications to studies of the nanocrystal surface. *J. Phys. Chem.* **98**, 4109–4117 (1994).
19. Taylor, J., Kippeny, T. & Rosenthal, S. J. Surface stoichiometry of CdSe nanocrystals determined by Rutherford backscattering spectroscopy. *J. Clust. Sci.* **12**, 571–582 (2001).
20. Sachleben, J. R. et al. NMR studies of the surface structure and dynamics of semiconductor nanocrystals. *Chem. Phys. Lett.* **198**, 431–436 (1992).
21. Becerra, L. R., Murray, C. B., Griffin, R. G. & Bawendi, M. G. Investigation of the surface morphology of capped CdSe nanocrystallites by 31 P nuclear magnetic resonance. *J. Chem. Phys.* **100**, 3297–3300 (1994).
22. Krauss, T. D. & Brus, L. E. Charge, polarizability, and photoionization of single semiconductor nanocrystals. *Phys. Rev. Lett.* **83**, 4840–4843 (1999).
23. Gao, F., Bajwa, P., Nguyen, A. & Heyes, C. D. Shell-dependent photoluminescence studies provide mechanistic insights into the off–grey–on transitions of blinking quantum dots. *ACS Nano* **11**, 2905–2916 (2017).
24. Verberk, R., van Oijen, A. M. & Orrit, M. Simple model for the power-law blinking of single semiconductor nanocrystals. *Phys. Rev. B* **66**, 233202 (2002).
25. Müller, J. et al. Air-induced fluorescence bursts from single semiconductor nanocrystals. *Appl. Phys. Lett.* **85**, 381–383 (2004).
26. Protesescu, L. et al. Nanocrystals of cesium lead halide perovskites ($CsPbX_3$, X=Cl, Br, and I): novel optoelectronic materials showing bright emission with wide color gamut. *Nano Lett.* **15**, 3692–3696 (2015).
27. Swarnkar, A. et al. Colloidal $CsPbBr_3$ perovskite nanocrystals: luminescence beyond traditional quantum dots. *Angew. Chem.* **127**, 15644–15648 (2015).
28. Cazaux, J. The electric image effects at dielectric surfaces. *IEEE Trans. Dielectr. Electr. Insul.* **3**, 75–79 (1996).
29. Berrettini, M. G., Braun, G., Hu, J. G. & Strouse, G. F. NMR Analysis of Surfaces and Interfaces in 2-nm CdSe. *J. Am. Chem. Soc.* **126**, 7063–7070 (2004).
30. Gomes, R. et al. Binding of phosphonic acids to CdSe quantum dots: a solution NMR study. *J. Phys. Chem. Lett.* **2**, 145–152 (2011).
31. Hens, Z. & Martins, J. C. A solution NMR toolbox for characterizing the surface chemistry of colloidal nanocrystals. *Chem. Mater.* **25**, 1211–1221 (2013).
32. Ammann, C., Meier, P. & Merbach, A. A simple multinuclear NMR thermometer. *J. Magn. Reson. (1969)* **46**, 319–321 (1982).
33. Yu, W. W., Qu, L., Guo, W. & Peng, X. Experimental determination of the extinction coefficient of CdTe, CdSe, and CdS nanocrystals. *Chem. Mater.* **15**, 2854–2860 (2003).
34. Jasieniak, J., Smith, L., Van Embden, J., Mulvaney, P. & Califano, M. Re-examination of the size-dependent absorption properties of CdSe quantum dots. *J. Phys. Chem. C.* **113**, 19468–19474 (2009).
35. Fritzinger, B., Capek, R. K., Lambert, K., Martins, J. C. & Hens, Z. Utilizing self-exchange to address the binding of carboxylic acid ligands to CdSe quantum dots. *J. Am. Chem. Soc.* **132**, 10195–10201 (2010).
36. Hassinen, A., Moreels, I., de Mello Donegá, C., Martins, J. C. & Hens, Z. Nuclear magnetic resonance spectroscopy demonstrating dynamic stabilization of CdSe quantum dots by alkylamines. *J. Phys. l Chem. Lett.* **1**, 2577–2581 (2010).
37. Morris-Cohen, A. J., Malicki, M., Peterson, M. D., Slavin, J. W. & Weiss, E. A. Chemical, structural, and quantitative analysis of the ligand shells of colloidal quantum dots. *Chem. Mater.* **25**, 1155–1165 (2012).
38. Lizhi, H., Toyoda, K. & Ihara, I. Dielectric properties of edible oils and fatty acids as a function of frequency, temperature, moisture and composition. *J. Food Eng.* **2**, 151–158 (2008).
39. Flory, P. J. *Principles of polymer chemistry*. (Cornell University Press, New York, 1953).
40. Li, H., Qian, C.-J., Sun, L.-Z. & Luo, M.-B. Conformational properties of a polymer tethered to an interacting flat surface. *Polym. J.* **42**, 383 (2010).
41. Li, J. J. et al. Large-scale synthesis of nearly monodisperse CdSe/CdS core/shell nanocrystals using air-stable reagents via successive ion layer adsorption and reaction. *J. Am. Chem. Soc.* **125**, 12567–12575 (2003).
42. Nilsson, M. The DOSY toolbox: a new tool for processing PFG NMR diffusion data. *J. Magn. Reson.* **200**, 296–302 (2009).
43. Pelta, M. D., Morris, G. A., Stchedroff, M. J. & Hammond, S. J. A one-shot sequence for high-resolution diffusion-ordered spectroscopy. *Magn. Reson. Chem.* **40**, 147–152 (2002).

Acknowledgements

Electron microscopy was peformed by Dr. C. Ducati and Dr. F. Wisnivesky-Rocca-Rivarola at the University of Cambridge, Department of Materials Science and Metallurgy, for which we are immensely grateful. ICP-MS measurements were kindly performed by Chris Dadswell. XRD measurements were acquired with assistance from the Chen group at Sussex.

Author contributions

A.A.E.F. conducted synthetic methodologies reported, recorded UV-Vis measurements and made significant contribution to manuscript preparation. M.A.O. conceived the CTST model and performed simulations reported and made a substantial contribution to manuscript preparation. I.J.D. and G.L.A. performed and processed raw NMR data and assisted with the interpretation thereof.

Additional information

Supplementary information accompanies this paper at https://doi.org/10.1038/s42004-019-0164-x.

Competing interests: The authors declare no competing interests.

Reprints and permission information is available online at http://npg.nature.com/reprintsandpermissions/

Publisher's note: Springer Nature remains neutral with regard to jurisdictional claims in published maps and institutional affiliations.